



Microkinetic modeling of steady-state NO/H₂/O₂ on Pt/BaO/Al₂O₃ NO_x storage and reduction monolith catalysts[☆]

Jin Xu, Michael P. Harold^{*}, Vemuri Balakotaiah^{**}

Department of Chemical & Biomolecular Engineering, University of Houston, Houston, TX 77204-4004, United States

ARTICLE INFO

Article history:

Received 14 August 2008

Received in revised form 1 November 2008

Accepted 12 November 2008

Available online 21 November 2008

Keywords:

NO_x
Hydrogen
Platinum
Barium
Selective catalytic reduction
NO_x storage and reduction
Lean NO_x trap

ABSTRACT

A steady-state microkinetic model for NO reduction by H₂ and NH₃ in O₂ on alumina supported Pt/BaO monolith catalysts is developed based on the measurements from a parallel experimental study (R. Clayton, M.P. Harold, V. Balakotaiah, Selective catalytic reduction of NO by H₂ in O₂ on Pt/BaO/Al₂O₃, Appl. Catal. B: Environ. 81 (3–4) (2008) 161–18). The microkinetic model describes pertinent Pt-catalyzed regeneration chemistry during NO_x storage and reduction with H₂. Kinetic parameters not available from the literatures are estimated to capture the experimental trends and to meet thermodynamic constraints. The kinetic model is incorporated into a short monolith reactor model to simulate the steady-state NH₃/O₂, NH₃/NO and NO/NH₃/H₂ reaction systems. The predicted conversion and product distribution are in excellent qualitative and good quantitative agreement with the experimental data. Among other features, the model predicts for the three reaction systems the non-linear light-off, and the product selectivity dependencies on temperature and feed composition. The model predicted trends in the species surface coverages with operating conditions help to elucidate the selectivity trends. A sensitivity analysis of the rate constants identified the critical steps in the reaction network. The effects of external mass transfer on the conversions and product distributions are assessed and discussed.

© 2008 Elsevier B.V. All rights reserved.

1. Introduction

The emission of NO_x from diesel and lean burn gasoline engines is a major mobile precursor source of ground-level ozone. Lean burn NO_x cannot be efficiently abated by the conventional three way catalytic (TWC) converter, which was specifically designed for stoichiometric vehicle engines. Technologies under development to meet the increasingly stringent NO_x regulations are exhaust gas recirculation (EGR) [1], selective catalytic reduction (SCR) with

ammonia/urea [2] or hydrocarbons [3], and NO_x storage and reduction (NSR), the subject of this study.

First proposed in the 1990s [4], NSR is a periodically operated catalytic process involving two alternating phases in the lean NO_x trap (LNT), the reactor in which NSR occurs. The LNT contains a multi-functional monolith catalyst comprising precious metal (Pt and Rh) and an alkaline-earth metal oxide (e.g. BaO) supported on a high surface area support (γ-Al₂O₃). During the lean phase, exhaust NO_x in the presence of excess oxygen is stored on the metal oxides in the form of nitrites and nitrates for 30–90 s to avoid any significant NO_x breakthrough. Then either the engine is run rich or reductant is injected into the exhaust stream to produce a rich mixture for a much shorter duration than the storage (3–10 s). This rich phase serves to reduce the stored NO_x and regenerate the NSR catalyst for the use of the next cycle. During the rich phase, the NO_x trap operates much like a TWC converter, but with a much heavier duty due to the enrichment of NO_x in the system during the previous lean operation. In addition to being the NO_x reduction catalyst, Pt also catalyzes NO oxidation reaction forming NO₂, which is a crucial step for NO_x storage during the lean phase [5,6]. In order to achieve efficient NO_x storage and reduction, rather high Pt loadings (1–2 wt%) are needed in comparison to less than 0.2% in typical TWC converters [6]. While the feasibility of NSR processes has been demonstrated and now commercialized [7], further

[☆] This report was prepared as an account of work sponsored by an agency of the United States Government. Neither the United States Government nor any agency thereof, nor any of their employees, makes any warranty, express or implied or assumes any legal liability or responsibility for the accuracy, completeness, or usefulness of any information, apparatus, product, or process disclosed, or represents that its use would not infringe privately owned rights. References herein to any specific commercial product, process, or service by trade name, trademark, manufacturer, or favoring by the United States Government or any agency thereof. The views and opinions of authors expressed herein do not necessarily state or reflect those of the United States Government or any agency thereof.

^{*} Corresponding author at: Department of Chemical & Biomolecular Engineering, S-222 Engineering Bldg 1, University of Houston, Houston, TX 77204-4004, United States. Tel.: +1 7137434307; fax: +1 7137434323.

^{**} Corresponding author.

E-mail addresses: mharold@uh.edu (M.P. Harold), bala@uh.edu (V. Balakotaiah).

Nomenclature

A	pre-exponential kinetic constant ($\text{mol s}^{-1} \text{m}^{-3}$)
C_T	gas phase concentration (mol m^{-3})
C_{Pt}	Platinum loading (mol/m^3 washcoat)
D_m	molecular diffusivity ($\text{m}^2 \text{s}^{-1}$)
E	activation energy (kJ mol^{-1})
k	kinetic constant ($\text{mol s}^{-1} \text{m}^{-3}$)
k_c	mass transfer coefficient (m s^{-1})
L	monolith length (m)
R	universal gas constant, $8.314\text{E}-3 \text{ kJ mol}^{-1} \text{K}^{-1}$; reaction rate ($\text{mol m}^{-3} \text{s}^{-1}$)
R_Ω	effective transverse length scale (m)
S_N	stoichiometric number of the feed defined by Eq. (16)
S_0	sticking coefficient at 0 coverage
T	Temperature (K)
$\langle u_f \rangle$	mean fluid velocity (m s^{-1})
X	mole fraction

Greek letters

α_v	platinum surface area per unit washcoat volume (m^2/m^3 washcoat)
δ_c	washcoat thickness (m)
θ	fractional coverage of surface species
ρ	density (kg m^{-3})
τ_c	residence time (s)

Subscripts

ad	adsorption
c	consumption of surface species
de	desorption
f	feed; forward reaction
g	generation of surface species
i	index of gaseous component
j	index of surface species
k	index of micro-reaction steps
m	bulk phase
r	backward reaction
s	solid phase

optimization to achieve high NOx conversion and N_2 selectivity with minimal fuel penalty requires a deep understanding of the catalytic chemistry and kinetics and their coupling with mass and heat transfer processes.

The role of hydrogen is particularly important in NOx storage and reduction. While a typical lean burn gasoline exhaust contains CO/H_2 of about 3 supplemented by low molecular weight hydrocarbons, and a typical diesel exhaust contains an even higher level of hydrocarbons, H_2 can be catalytically generated in the LNT by the water gas shift reaction and steam reforming of exhaust hydrocarbons. Moreover, H_2 has been shown to be the most effective reductant in terms of reducing stored NOx, albeit to a mixture of N_2 , N_2O , and NH_3 . While NH_3 is normally considered an unfavorable byproduct, more recent technologies exploit this drawback by combining the NOx trap with SCR [8–11]. In the Mercedes E320 ‘Bluetec’ model, DaimlerChrysler applied a new exhaust after treatment system including both the NOx adsorption catalyst (NAC) and an SCR catalyst. This model is able to achieve the ‘Tier 2 Bin 8’ emission levels required for 45 of the 50 states

[8]. Hemingway [9] and Hu [10] proposed similar technology to utilize NH_3 from the NOx trap to further reduce NOx in a downstream SCR. For these reasons, understanding the NOx reduction by H_2 chemistry in the presence of O_2 is essential.

NO reduction by H_2 on precious metal catalysts has been extensively studied since the TWC development era in the 1970s. It was shown that H_2 is a superior reductant of NO, igniting at low temperature on precious metal catalysts [12–16]. Previous NO/ H_2 on Pt works were reviewed in our earlier paper [17]. In that study we investigated the performance of steady-state anaerobic NO reduction by H_2 on Pt/BaO/ Al_2O_3 monolith catalysts over a wide temperature and concentration range. Three N-containing products, N_2O , N_2 , and NH_3 were observed with the selectivities depending on temperature and feed composition. At low temperature, NO was partially reduced to N_2O . In the intermediate temperature range, complete NO conversion was achieved with selectivities mainly determined by H_2/NO feed ratio. High selectivity to N_2 was obtained with H_2/NO ratio close to 1, while NH_3 was the major product for H_2/NO ratio greater than 1.5. Temperatures higher than 350°C are favorable to N_2 production due to the emergence of NH_3 decomposition.

Recently, ammonia has been reported to serve as a hydrogen carrier and reductant of stored NOx on Pt/Ba catalysts [18]. Once formed upstream under conditions of high H_2/NO ratio, NH_3 can react with either gas phase NO or stored NOx downstream. Thus, the reduction of NO by NH_3 is an important reaction during NOx storage and reduction. It has been reported that NO reduction by NH_3 produces N_2O , in addition to the favorable N_2 production, both in the absence of O_2 [19,20] and presence of O_2 [21,22]. Otto et al. [20,23] studied the NO/ NH_3 reaction by nitrogen-15 isotope labeling and concluded that N_2O is predominantly formed by the reaction between NO molecules, while N_2 is formed by the reaction of adsorbed NH_3 and NO. Gland and Korchak [24] reported that the rate limiting step of the NO/ NH_3 reaction is the reaction between an adsorbed fragment of NH_3 and an adsorbed NO molecule. In both studies, a single site Langmuir–Hinshelwood kinetic model was used to describe the reaction rates.

The co-existence of H_2 and NH_3 during NSR has prompted recent studies to elucidate their roles. Cumaratunge et al. [18] proposed that stored NOx regeneration occurs by a moving front of H_2 . Experiments carried out using either NH_3 or H_2 as the reductant showed NH_3 to be as effective as H_2 at 300°C . In a more recent experimental study, Clayton et al. [25] conclusively showed the existence of H_2 and NH_3 fronts at sufficiently high temperature. They also showed that H_2 is a more effective reductant than NH_3 , especially at lower temperature. They observed that NH_3 conversion decreased almost linearly with the increase in the co-feed concentration of H_2 and was completely blocked when H_2/NO ratio reached 1:1. At a temperature of about 300°C , NO reduction by either of the reductants is fully ignited, whereas the temperature is not high enough for the activation of NH_3 decomposition.

The oxidation of ammonia on Pt may also be encountered under some conditions during NSR. This is likely to occur at the leading edge of the aforementioned NH_3 front where the Pt sites are still covered with O and NO species. Breen et al. [26] reported the production of N_2 during the lean storage phase, speculating the reaction between O_2 and adsorbed NH_3 . These findings were corroborated in the more recent study of Clayton et al. [27]. Platinum-catalyzed ammonia oxidation with 95–97% yields of NO at temperatures of $810\text{--}940^\circ\text{C}$ is one of the steps in the large-scale production of nitric acid. While the process has been commercialized for about a century and the reaction been extensively studied, the reaction mechanism and kinetics attract continued interest. The difficulties in studying the intrinsic kinetics arise from the high reaction rate at the elevated temperatures, complex product distribution and the reaction-induced restructuring of the catalyst

surface [28]. Most previous kinetic studies were focused on gauzes and foils, mainly because industrial NH_3 oxidation is carried out on Pt (90%)–Rh (10%) alloys (woven into gauzes). Recently, Clayton et al. [25] conducted NH_3 oxidation experiments in monolith reactors loaded with a Pt/BaO/ Al_2O_3 catalyst over the temperature range of 50–500 °C. A complex product mixture of N_2 , N_2O , NO, NO_2 and, of course, H_2O was observed. The steady-state product distribution was found strongly dependent on temperature and feed composition.

While most modeling studies during the early stage of NSR development were focused on the storage mechanisms [5,29,30], more attention is paid to the investigation of chemistry and kinetics in the reduction and regeneration operations. Kinetic models with a range of complexity have been reported. Xu et al. [17] developed a 13-step microkinetic model to account for all experimentally observed gas species during the steady-state reduction of NO by H_2 . The microkinetic model, consisting of both elementary and lumped steps, was incorporated into a “short monolith” reactor model, which emphasizes mass transfer effects while assuming complete back mixing, to simulate conversions and product selectivities during anaerobic NO reduction by H_2 on Pt/BaO/ Al_2O_3 catalysts. The model predictions successfully captured all major experimental trends. In a recent study by Larson et al. [31], a 28-step model was proposed to describe the chemistry of catalytic NOx reduction by H_2 and CO in the presence of O_2 . The kinetic model was substituted into a fluid model that accounts for axial gradients but neglects external mass transfer effects. The reaction model, comprising about 80 kinetic parameters, was fit to a set of experimental data taking into account thermodynamic constraints. More recently, Koci et al. [32] developed a kinetic model consisting of global reactions to study the dynamics and selectivity of NOx reduction on NSR catalysts. A more detailed kinetic model accounting for CO_2 and H_2O effects was presented by Lindholm et al. [33].

The objective of the current study is to extend our previous microkinetic model to a reaction mixture containing O_2 [17]. We develop a kinetic model consisting of both elementary and lumped reaction steps that are needed to predict the conversion and selectivity trends reported in recent experimental study [25]. The model predictions of conversions and product distributions are compared with experimental results of three steady-state systems: NH_3/O_2 , NH_3/NO and $\text{NH}_3/\text{H}_2/\text{NO}$. The model predicted trends in the gas phase and surface species help to elucidate the trends in the conversions and selectivities. The effects of external mass transfer on the conversions and product distributions are assessed and discussed. The paper is organized as follows. After we describe the reactor model and equations we develop the expanded microkinetic model based on experimental trends. This is followed by a thermodynamic constraint analysis and kinetic parameter considerations. We then compare the reactor model simulations with experimental data and utilize the model predictions to elucidate the chemistry and reactor performance.

2. Model description

2.1. Reactor model

A short monolith model is used to validate the proposed microkinetic model for NO reduction by H_2 and NH_3 with the presence of O_2 . Balakotaiah et al. [34] developed a “short monolith reactor” model (SMR) and examined it with simple reaction systems. The SMR model is obtained by integrating the conventional integral reactor model along the axial direction and applying boundary conditions. The SMR qualitatively captures the main trends of an integral reactor with axial gradients and is quantitatively accurate for a short reactor with negligible axial

Table 1

Physical properties and reactor parameters used in simulations.

k_{c,H_2}	0.251 (m/s)
$k_{c,\text{NO}}$	0.068 (m/s)
k_{c,NH_3}	0.095 (m/s)
ρ_f	0.854 (kg/m ³)
τ_c	0.08 (s)
α_v	1.5E6 (m ² Pt/m ³ washcoat)
δ_c	2.0E–5 (m)
k_{c,O_2}	0.069 (m/s)
k_{c,NO_2}	0.060 (m/s)
$k_{c,\text{N}_2\text{O}}$	0.062 (m/s)
C_T	30.5 (mol/m ³)
R_Ω	5E–4 (m)
C_{Pt}	40 (mol Pt/m ³ washcoat)

gradients. In a recent study, Xu et al. [17] compared the SMR model with an integral lumped thermal model (axial concentration gradients with uniform temperature) for the NO/ H_2 reaction system. The SMR model was shown to adequately capture the main trends in the product distribution.

In addition to neglecting axial gradients, the following assumptions are made: (1) steady-state operation; (2) very thin washcoat with no diffusion limitations; (3) constant physical properties; (4) laminar flow in the monolith channel. With these assumptions, the SMR consists of algebraic equations, describing a set of material balances. The fluid species balances are given by

$$\frac{(X_{i,m} - X_{i,f})}{\tau_c} + \frac{k_{c,i}}{R_\Omega} (X_{i,m} - X_{i,s}) = 0 \quad (1)$$

where X_i is the mole fraction of component i (subscripts, m , s and f denote to fluid (cup-mixing), solid and feed, respectively), $\tau_c (=L/\langle u_f \rangle)$ is the residence time, R_Ω is the hydraulic radius defined as the ratio of the channel area to channel perimeter, $k_{c,i}$ is the mass transfer coefficient of component i , equal to $D_{m,i}/R_\Omega$, and $D_{m,i}$ is the molecular diffusivity. [Remark: channel hydraulic diameter is $4R_\Omega$.] The balances for the gas phase species present in the catalyst phase are given by

$$\delta_c \left(\sum R_{i,ad} - \sum R_{i,de} \right) - C_T k_{c,i} (X_{i,m} - X_{i,s}) = 0 \quad (2)$$

where δ_c is the washcoat thickness, C_T is the total gas phase concentration, and $R_{i,ad}$ and $R_{i,de}$ are the adsorption and desorption rates of component i at the catalyst surface. The adsorbed species balances in the catalyst phase are given by:

$$\sum_j (R_{j,c} - R_{j,g}) = 0 \quad (3)$$

where c (g) denotes consumption (generation). The kinetic model is described in the next section. We assume that the total number of active platinum sites is conserved and the sites are equally accessible to all surface species:

$$\sum_j \theta_j + \theta_v = 1 \quad (4)$$

where the subscript v refers to vacant sites and the summation is over all surface species.

A more detailed model description of the SMR can be found elsewhere [17]. Physical properties and reactor parameters used in the simulations are provided in Table 1.

2.2. Microkinetic model

In a previous study [17], we developed a microkinetic model for anaerobic NO reduction by H_2 on alumina-supported Pt. The model consists of 13 reaction steps, accounting for all major products, NO_2 , N_2O , N_2 , NH_3 and H_2O :

S1	$\text{NO} + \text{Pt} \leftrightarrow \text{NO} - \text{Pt}$
S2	$\text{H}_2 + 2\text{Pt} \leftrightarrow 2\text{H} - \text{Pt}$
S3	$\text{NO} - \text{Pt} + \text{H} - \text{Pt} \leftrightarrow \text{N} - \text{Pt} + \text{OH} - \text{Pt}$
S4	$\text{N}_2\text{O} + 2\text{Pt} \leftrightarrow \text{N} - \text{Pt} + \text{NO} - \text{Pt}$
S5	$\text{H} - \text{Pt} + \text{O} - \text{Pt} \leftrightarrow \text{OH} - \text{Pt} + \text{Pt}$
S6	$\text{H} - \text{Pt} + \text{OH} - \text{Pt} \leftrightarrow \text{H}_2\text{O} + 2\text{Pt}$
S7	$\text{N}_2 + 2\text{Pt} \leftrightarrow 2\text{N} - \text{Pt}$
S8	$\text{NO} - \text{Pt} + \text{Pt} \leftrightarrow \text{N} - \text{Pt} + \text{O} - \text{Pt}$
S10	$\text{N} - \text{Pt} + 3\text{H} - \text{Pt} \leftrightarrow \text{NH}_3 - \text{Pt} + 3\text{Pt}$
S13	$\text{NH}_3 + \text{Pt} \leftrightarrow \text{NH}_3 - \text{Pt}$
S14	$\text{O}_2 + 2\text{Pt} \leftrightarrow 2\text{O} - \text{Pt}$
S15	$\text{NO} - \text{Pt} + \text{O} - \text{Pt} \leftrightarrow \text{NO}_2 - \text{Pt} + \text{Pt}$
S16	$\text{NO}_2 + \text{Pt} \leftrightarrow \text{NO}_2 - \text{Pt}$

The reaction indices correspond to those in the previous study, noting that in the development steps S9, S11 and S12 were eliminated.

The NO/H₂ microkinetic model was shown to capture most experimental trends under anaerobic conditions, particularly under rich conditions (H₂/NO > 1). Justification for the reaction steps involved in H₂O and N₂ formation were described in detail and will not be repeated here. However, there are a few points regarding N₂O, NO₂, and NH₃ that will benefit from some review.

- The formation of N₂O occurs through the reaction of N and NO surface species (reverse reaction of step S4). The low temperature formation of N₂O involving NO bond scission reaction by H adatoms (S3) has a lower activation barrier. N₂O can decompose via the forward reaction of S4 which, combined with the direct NO bond scission, helps to account for the reduced selectivity to N₂O at higher temperatures.
- The formation of NO₂ is by oxidation of NO adspecies (S15). This reaction is obviously more important in the aerobic system and will be addressed below.
- The formation of NH₃ occurs by sequential addition of H to N adatoms, which is consolidated into a single reversible reaction, S10. High H₂/NO feeds favor the production of NH₃. The reverse of reaction S10 provides ammonia decomposition at higher temperature. In the aerobic system, the absence of O₂ in the feed means that NH₃ was consumed only by decomposition. Previous studies have shown that NH₃ decomposes at temperatures exceeding 350 °C [17,33,34].

The current study is aimed at further investigating Pt-catalyzed NH₃ oxidation chemistry through the reaction of NH₃ with O₂ and NO. As in the previous study, the current study is not aimed to pursuing a reaction network consisting of truly elementary reactions. Rather, our objective is to develop a kinetic model that contains a minimum number of reaction steps and species yet is comprehensive enough to explain all the important experimental trends. We explain additions to the anaerobic microkinetic model based on experimental findings described in a previous study and highlighted here.

Fig. 1 shows experimental steady-state light-off curves of NH₃ oxidation over a range of O₂ feed concentrations [25]. It is seen that NH₃ oxidation ignites at about 150 °C and the ignition temperature is rather insensitive to the O₂ concentration, although a slight inhibitive effect of O₂ is apparent. As mentioned, anaerobic NH₃ decomposition occurs at much higher temperature. Clearly then, reactions involving surface oxygen species are involved in the scission of the NH_x (x = 1, 2, 3) bonds at low temperature. The dissociative adsorption of gas phase O₂ (S14) provides the O adatoms for the oxidation of adsorbed NH₃ and H, both of which produce OH adspecies which can further react with adsorbed NH₃.

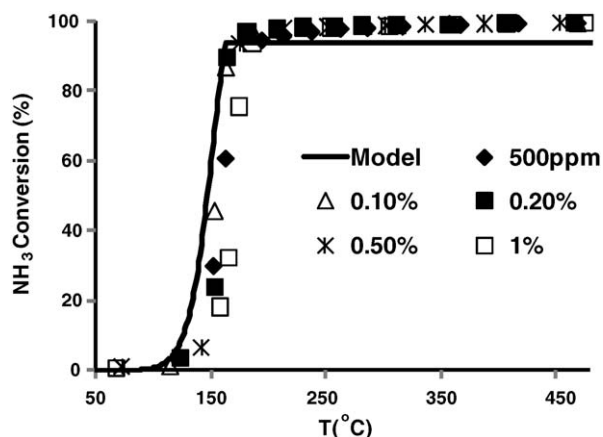
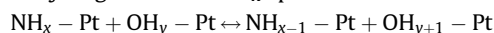
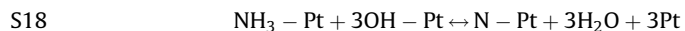
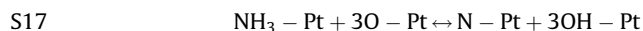


Fig. 1. Steady-state light-off curve of NH₃ oxidation. NH₃ concentration is fixed at 500 ppm. Various points are experimental data for different feed oxygen concentrations. The solid line is model predictions for O₂ concentration of 0.2%. The light-off curve is not sensitive to O₂ concentration as long as it is in excess.

Consider the general reaction expression involving the oxidative dehydrogenation of NH_x species with O–Pt and OH–Pt:

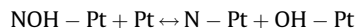
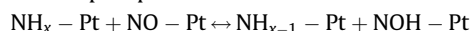


where x = 1, 2, 3 and y = 0, 1. In order to reduce the complexity of this set of six reactions, we consider two lumped reactions between adsorbed NH₃ and O–Pt and OH–Pt:

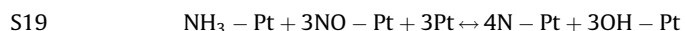


These are obviously not elementary steps, but are steps that lump the complete oxidative dehydrogenation of NH₃ by O–Pt (S17) and OH–Pt (S18), respectively. S17 involves the abstraction of H from NH_x–Pt by O–Pt, producing OH–Pt, which can then abstract additional H atoms to form water in S18.

As mentioned earlier, NO reduction by NH₃ is an important sequential reaction in either the anaerobic or aerobic system. Fig. 2 shows experimental steady-state conversion and product distribution of NO reduction by excess NH₃ as a function of temperature. The ignition temperature is at about 170 °C. That both NO and NH₃ decomposition require higher temperature means that a reaction pathway involving the direct oxidation of NH₃ by NO is needed [25]. Here we postulate a concerted mechanism that involves the scission of NO by H, involving the two-step sequence:



where x = 1, 2, 3. Ford et al. [35] calculated that the preferred route for NOH–Pt decomposition is to NO–Pt + H–Pt although N–Pt + OH–Pt is only slightly less favorable. The formation of HNO–Pt is also plausible, with the favored decomposition products being NH–Pt and O–Pt [35]. Following the approach we used for steps S17 and S18, we propose the following lumped step involving complete oxidative dehydrogenation of NH₃ by NO–Pt:



In another experiment, the reactivities of H₂ and NH₃ as reductants of NO were compared [25]. Fig. 3 shows the steady-state effluent composition of a NO/H₂/NH₃ feed (500 ppm of each component) as a function of temperature. An interesting finding was that the NH₃ effluent concentration exceeded the feed concentration over the 100–180 °C temperature range; i.e. NH₃

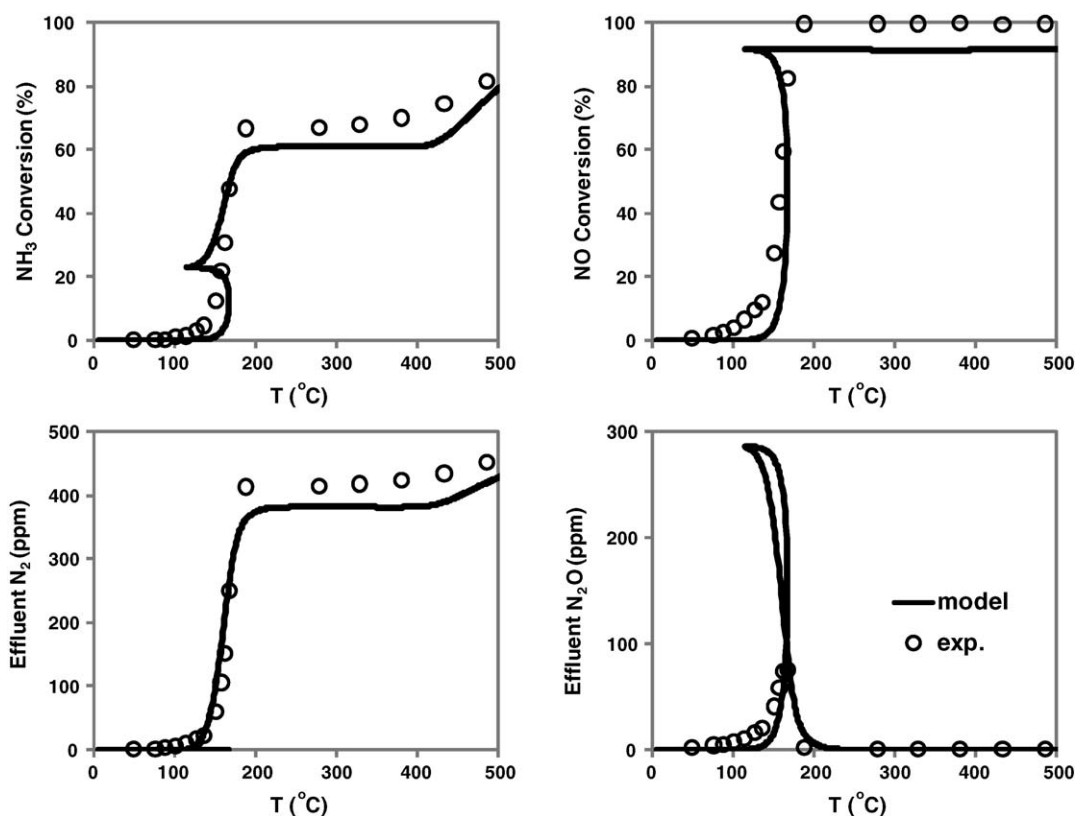
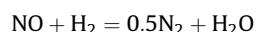
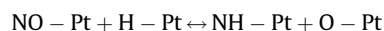


Fig. 2. Steady-state NO reduction by equal molar NH_3 (500 ppm each) as a function of temperature. Circle points are experimental data. Solid lines are model predictions.

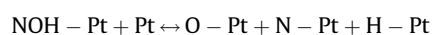
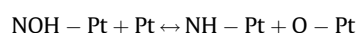
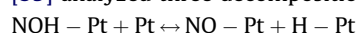
was actually produced rather than consumed. [Remark: Similar chemistry was observed in the anaerobic NO/H_2 system for H_2/NO ratio close to unity in [17], but was considered a secondary trend in that study and was not considered during the model development.] These data indicate that H_2 is a more effective reductant of NO than NH_3 . The same study [17] showed that an equimolar feed of H_2 and NO favored the production of N_2 according to the overall reaction:



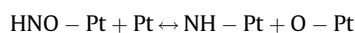
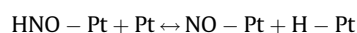
For example, at 100 °C the selectivity to N_2 is 98%. Thus, that any ammonia was produced in the ternary feed experiment indicates a reaction pathway involving adsorbed NO and H that competes with N_2 and H_2O formation within this temperature range. The production of NH_3 cannot be explained by the coupling of reactions S3 ($\text{NO} - \text{Pt} + \text{H} - \text{Pt} \leftrightarrow \text{N} - \text{Pt} + \text{OH} - \text{Pt}$) and S10 ($\text{N} - \text{Pt} + 3\text{H} - \text{Pt} \leftrightarrow \text{NH}_3 - \text{Pt} + 3\text{Pt}$). H_2O formation is the preferred product of $\text{H} - \text{Pt}$ in the presence of $\text{OH} - \text{Pt}$; i.e. OH and N formed simultaneously in S3 will instead produce N_2 and H_2O . Thus, we propose a reaction step that is parallel to S3:



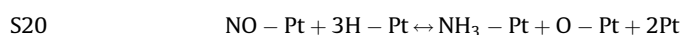
As mentioned above, the $\text{NOH} - \text{Pt}$ and $\text{HNO} - \text{Pt}$ intermediates have been proposed and analyzed in the literature [35,36]. Ford et al. [35] analyzed three decomposition pathways for $\text{NOH} - \text{Pt}$:



Similarly, two pathways were analyzed for $\text{HNO} - \text{Pt}$:



The $\text{NH} - \text{Pt}$ product may be further hydrogenated to form NH_3 . We again consolidate the $\text{NH} - \text{Pt}$ formation step with sequential addition of two $\text{H} - \text{Pt}$, with the result being:



As we show below, not only can S20 be used to predict the intermediate temperature formation of NH_3 , the reverse of S20 provides another route for NH_3 oxidation.

2.3. Thermodynamic constraints

The previous section showed the expansion of the 13-step microkinetic model for the NO/H_2 system with the additional four lumped reaction steps (S17–S20) for $\text{NO}/\text{H}_2/\text{O}_2$. Activation energies determine the relative magnitudes of competing reactions of complex systems with multiple products at different temperatures. Hence, their values are crucial in determining the main experimental trends. In the previous study of the NO/H_2 system [17], we introduced how standard enthalpy change of an overall reaction can be used as a constraint in a microkinetic model. In this section, we apply the same method in the expanded microkinetic model to estimate additional activation energies, keeping with the assumption from [17] that the temperature dependencies of enthalpies can be ignored. Later in the section we consider entropic constraints to estimate selected pre-exponential factors.

In the 17-step microkinetic model, there are five gaseous compounds: NO_2 , NO , N_2O , NH_3 , and H_2O . For each of these species we can define a linearly independent overall reaction with a prescribed enthalpy change; i.e. eight molecular species with three distinct atomic species gives five linearly independent reactions. As a result, five enthalpic constraints can be derived and utilized.

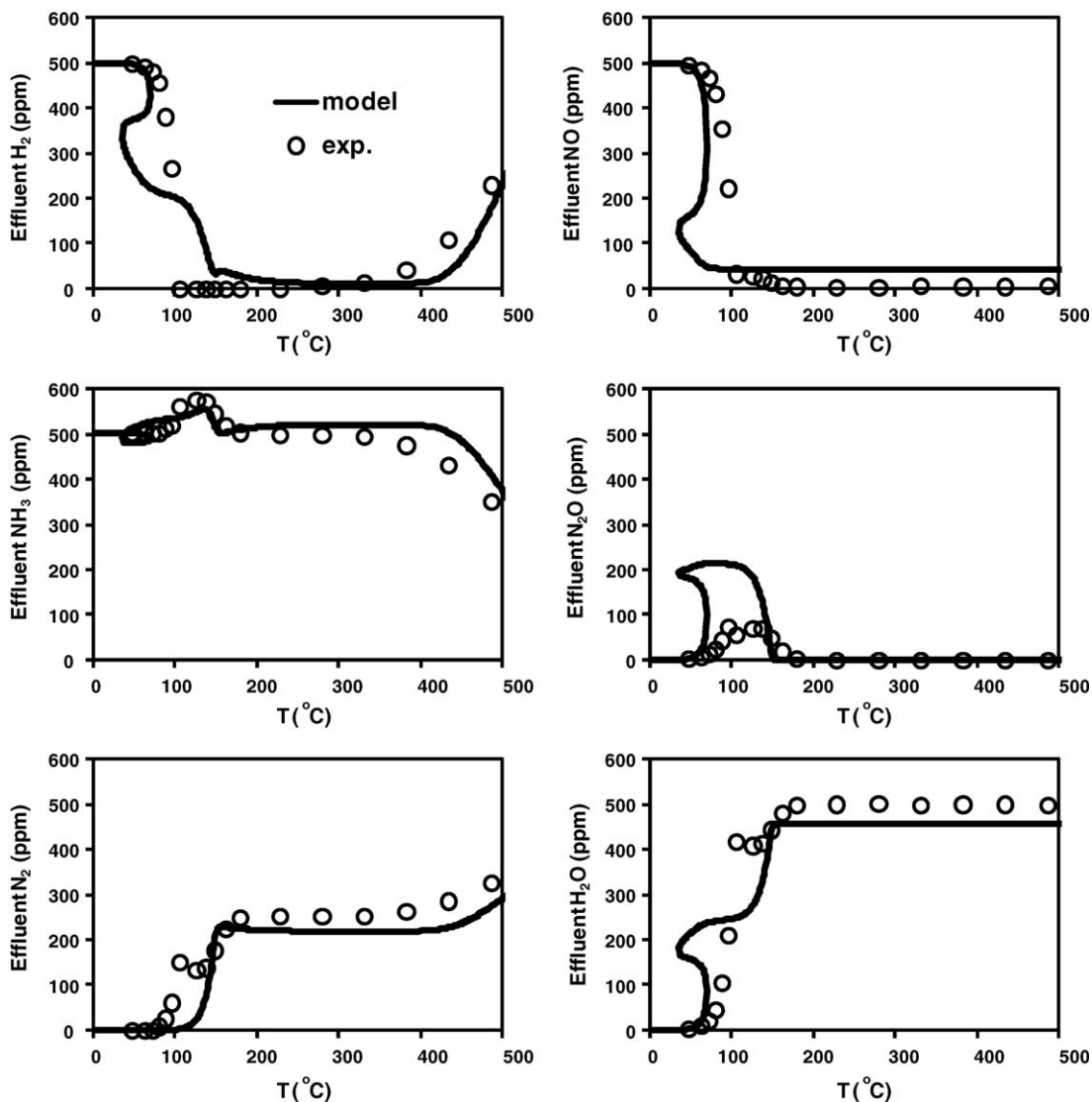
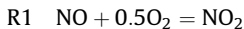


Fig. 3. Effluent concentrations during steady-state NO reduction by equal molar NH_3 and H_2 (500 ppm each) as a function of temperature. Circle points are experimental data. Solid lines are model predictions.

We begin the analysis with NO_2 formed by the oxidation of NO. The overall reaction is



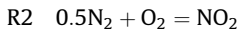
which satisfies the following stoichiometric relation:

$$\text{R1} = \text{S1} + 0.5\text{S14} + \text{S15} - \text{S16} \quad (5)$$

The activation energies of each of the steps on the right-hand side have been determined in a previous NOx storage study [30]. The ΔH of each reaction step can be calculated by

$$\Delta H_k = E_{k,f} - E_{k,r} \quad (6)$$

Substituting the activation energies from [30], the calculated ΔH of R1 is -57.2 kJ/mol, exactly the enthalpy difference between NO_2 and NO. This shows that the parameter set satisfies the thermodynamic constraint. Another overall reaction for NO_2 formation can be written as

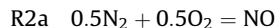


which satisfies the following stoichiometric relation:

$$\text{R2} = 0.5\text{S7} + \text{S14} - \text{S8} + \text{S15} - \text{S16} \quad (7)$$

The standard enthalpy of formation of NO_2 is 33.1 kJ/mol, while $E_{8,f}$ and $E_{8,r}$ are available from the literature [5,37]. The energy barrier for N_2 desorption, $E_{7,r}$, was estimated to be 130 kJ/mol to capture the experimental trends (113.9 kJ/mol by Vajo et al. [37]). Using Eq. (7), $E_{7,f}$, the activation energy of N_2 adsorption on Pt, is calculated to be 219.5 kJ/mol. This high value indicates that N_2 adsorption can be ignored and that N adatom recombination (reverse of S7) may be considered irreversible.

Now, we consider the overall reaction for NO formation:

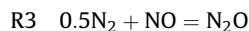


which satisfies the following stoichiometric relation:

$$\text{R2a} = 0.5\text{S7} + 0.5\text{S14} - \text{S8} - \text{S1} \quad (8)$$

Since R2a is a linear combination of R1 and R2 ($\text{R2a} = \text{R2} - \text{R1}$), this is not a new constraint. Substitution of the activation energies that satisfy constraints of R1 and R2 (Eqs. (5) and (7)) automatically satisfies Eq. (8).

An overall reaction of N_2O formation is given as

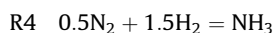


which satisfies the following stoichiometric relation:

$$R3 = 0.5S7 + S1 - S4 \quad (9)$$

R3 is linearly independent of R1 and R2, and is therefore an additional thermodynamic constraint. The ΔH for R3 can be calculated from thermodynamic data (-8.2 kJ/mol). Given ΔH values of steps S7 and S1, ΔH of reversible step S4 is calculated to be -61.8 kJ/mol. If we further assume the energy barrier for N_2O formation ($E_{4,r}$) to be 85.8 kJ/mol according our previous study [17], then the activation energy of adsorptive N_2O decomposition, $E_{4,f}$, must be 24 kJ/mol in order to satisfy Eq. (9).

The overall reaction of NH_3 formation is

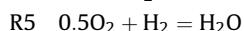


which satisfies the following stoichiometric relation:

$$R4 = 0.5S7 + 1.5S2 + S10 - S13 \quad (10)$$

Compared with exponential temperature dependence in the Arrhenius expression, adsorption rates of NH_3 and H_2 are relatively weak functions of temperature and the activation energies can be assumed to be zero. There are four activation energies left to be determined and three of them are independent. Activation energies of NH_3 formation and desorption, $E_{10,f}$ and $E_{13,r}$, were reported to be 48.4 and 117 kJ/mol by Vajo et al. [37]. We assign 146.5 kJ/mol to $E_{10,r}$, slightly lower than the value used in our previous NO/H_2 study (150.2 kJ/mol), to correctly predict NH_3 decomposition at high temperature range, which we show later. As a result, the H_2 desorption activation energy, $E_{2,r}$, is determined to be 73 kJ/mol, in the range of literature values (67 – 84 kJ/mol; an average of 72.8 kJ/mol [40]).

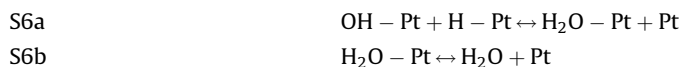
While step S6 is assumed irreversible in this study, an analysis of H_2O formation is carried out here for completeness. The overall reaction of H_2O formation is



which satisfies the following stoichiometric relation:

$$R5 = 0.5S14 + S2 + S5 + S6 \quad (11)$$

where S6 can be further divided into two steps:



$E_{5,f}$, $E_{5,r}$, $E_{6a,f}$, $E_{6a,r}$, $E_{6b,f}$, and $E_{6b,r}$ values are reported to be 11.5 , 74.9 , 17.4 , 73.6 , 40.3 and 0 kJ/mol, respectively, from the study by Deutschmann et al. [41]. In order to examine the consistency of the ΔH values of reversible steps S14 and S2 independently obtained in previous discussions, we calculate the overall enthalpy change of R5 using Eq. (11). The result is -241.6 kJ/mol, very close to the standard enthalpy of formation for gaseous H_2O , -241.8 kJ/mol. In this study, H_2O desorption is assumed to be instantaneous and irreversible. [Remark: the assumption of irreversibility for steps S6 and S7 eliminates the concentrations of H_2O and N_2 as model unknowns and simplifies the calculations.] However, the activation of H_2O on Pt, with a moderate activation energy of 73.6 kJ/mol, may be important to consider especially if CO is present and water gas shift chemistry occurs. However, we limit the current study to H_2 as the reductant.

There are in total 16 species in the microkinetic model, eight gas and eight surface species, comprising four elements; N, O, H and Pt. So far, we have discussed 12 steps (S1, S2, S4, S5, S6, S7, S8, S10, S13, S14, S15 and S16), which form a linearly independent reaction base set. Any additional reaction step not involving a new species (gas or surface) can therefore be described as a linear combination of the 12 base steps. The ΔH of such a linearly dependent reaction step is therefore determined and only one of its activation energies can be adjusted.

There are five remaining dependent steps in the 17-step microkinetic model described in Section 2.2. These can be expressed by the following:

$$S3 = S8 + S5$$

$$S17 = -S10 + 3S5$$

$$S18 = -S10 + 3S6$$

$$S19 = -S10 + 3S8 + 3S5$$

$$S20 = S8 + S10$$

Using ΔH values of the 12 independent steps, the ΔH values of the above five steps are calculated to be -83.7 , -160.7 , -27.4 , -221.6 and -49.8 kJ/mol, respectively. As mentioned before, the forward reactions of step S3 ($NO - Pt + H - Pt \leftrightarrow N - Pt + OH - Pt$) and S20 ($NO - Pt + 3H - Pt \leftrightarrow NH_3 - Pt + O - Pt + 2Pt$) account for N_2O and NH_3 formation, respectively, during the reduction of NO by H_2 . Since both overall reactions occur in the moderate temperature range of 100 – 180 °C (Fig. 3), an activation energy value of 60 kJ/mol is assigned to S3 and S20. The activation energies of the reverse reactions of S3 and S20 are then calculated to be 143.7 and 109.8 kJ/mol. The forward reaction of step S19 ($NH_3 - Pt + 3NO - Pt \leftrightarrow 4N - Pt + 3OH - Pt$), similar to that of S3, generates N adatoms, which are necessary for N_2O formation during the reduction of NO by NH_3 . Noticing the experimental finding that the ignition of the NO reduction by NH_3 reaction requires a higher temperature than that by H_2 , a higher value of 80 kJ/mol is assigned to $E_{20,f}$. Steps S17 ($NH_3 - Pt + 3O - Pt \leftrightarrow N - Pt + 3OH - Pt$) and S18 ($NH_3 - Pt + 3OH - Pt \leftrightarrow N - Pt + 3H_2O + 3Pt$) are lumped reaction steps to describe direct NH_3 oxidation (without NH_3 decomposition). Considering adsorbed O and OH species to be more active than NO adspecies for NH_3 oxidation, the activation energies of S17 and S18 are fixed at 40 and 30 kJ/mol, respectively. $E_{17,r}$, $E_{18,r}$ and $E_{19,r}$ are then calculated to be 200.7 , 57.4 and 301.6 kJ/mol. S17 and S19 are assumed irreversible due to the high reverse activation energies. While $E_{18,r}$ value is not high, step S18 is also assumed irreversible keeping with the assumption that H_2O is inert in this reaction system.

The standard enthalpies of formation of all gas species have been tabulated in thermodynamic handbooks. A subset consisting of 7 of the 12 independent reaction steps (S1, S2, S5, S8, S13, S14 and S16) can be used to calculate the standard formation enthalpy of the surface species. (Note: there are other options such as replacing S13 with S10.) It is straightforward to determine the standard enthalpy values of adsorbed O, H, NO, NO_2 and NH_3 by sorption experiments. On the other hand, determination of the values for adsorbed N and OH is difficult because N_2 is not easily dissociated on Pt and OH is a very active surface intermediate. The standard formation enthalpies of adsorbed N and OH are calculated to be 44.6 and -189.2 kJ/mol in this study. For comparison, Ford et al. [35] studied the adsorption of several atomic and molecular species and molecular fragments on Pt(111) using self-consistent periodic density functional theory (DFTGGA) calculations and the above two values were reported to be 44.9 and -144.0 kJ/mole, respectively.

In addition to enthalpic constraints there are entropic constraints. The former affects the activation energies while the latter affects the pre-exponential factors for simple Arrhenius rate expressions. The application of entropy (or, equivalently, Gibbs free energy) balance of an overall reaction requires that each of the reaction steps that it comprises is reversible and follows mass action kinetics. Thus, for lumped reaction steps that are either irreversible or do not follow mass action kinetics, entropic constraints cannot be applied. On the other hand, as shown above enthalpic constraints do not require these conditions.

Table 2
Rate expressions.

Step	Forward	Reverse
S1	$R_{1,f} = k_{1,f}(T)\theta_v X_{NO}$	$R_{1,r} = k_{1,r}(T)\theta_{NO}$
S2	$R_{2,f} = k_{2,f}(T)\theta_v X_{H_2,S}$	$R_{2,r} = k_{2,r}(T)\theta_{H_2}$
S3	$R_{3,f} = k_{3,f}(T)\theta_H \theta_{NO}$	$R_{3,r} = k_{3,r}(T)\theta_N \theta_{OH}$
S4	$R_{4,f} = k_{3,f}(T)\theta_v X_{N_2O,S}$	$R_{4,r} = k_{4,r}(T)\theta_{NO} \theta_N$
S5	$R_{5,f} = k_{5,f}(T)\theta_H \theta_O$	$R_{5,r} = k_{5,r}(T)\theta_v \theta_{OH}$
S6	$R_{6,f} = k_{6,f}(T)\theta_H \theta_{OH}$	Neglected
S7	Neglected	$R_{7,r} = k_{7,r}(T)\theta_N^2$
S8	$R_{8,f} = k_{8,f}(T)\theta_{NO} \theta_v$	$R_{8,r} = k_{8,r}(T)\theta_N \theta_O$
S10	$R_{10,f} = k_{10,f}(T)\theta_N \theta_H$	$R_{10,r} = k_{10,r}(T)\theta_v \theta_{NH_3}$
S13	$R_{13,f} = k_{13,f}\theta_v X_{NH_3,S}$	$R_{13,r} = k_{13,r}(T)\theta_{NH_3}$
S14	$R_{14,f} = k_{14,f}\theta_v^2 X_{O_2,S}$	$R_{14,r} = k_{14,r}(T)\theta_O^2$
S15	$R_{15,f} = k_{15,f}(T)\theta_{NO} \theta_O$	$R_{15,r} = k_{15,r}(T)\theta_{NO_2} \theta_v$
S16	$R_{16,f} = k_{16,f} X_{NO_2,S} \theta_v$	$R_{16,r} = k_{16,r}(T)\theta_{NO_2}$
S17	$R_{17,f} = k_{17,f}(T)\theta_O \theta_{NH_3}$	Neglected
S18	$R_{18,f} = k_{18,f}(T)\theta_{OH} \theta_{NH_3}$	Neglected
S19	$R_{19,f} = k_{19,f}(T)\theta_{NO} \theta_{NH_3}$	Neglected
S20	$R_{20,f} = k_{20,f}(T)\theta_{NO} \theta_H$	$R_{20,r} = k_{20,r}(T)\theta_O \theta_{NH_3}$

To illustrate, consider reaction step S3 which satisfies the stoichiometric relation $S3 = S8 + S5$. Since S3, S8 and S5 are each reversible and follow mass action rate expressions (Table 2), both enthalpic and entropic constraints can be applied. The ΔG of S3 is calculated to be 67.9 kJ/mol at the reference temperature 400 K using literature kinetic parameters of S3 and S5 (Table 3). As described in the next section, a pre-exponential value of 4.0×10^{14} mol/(s m³ washcoat) is assigned to the forward reaction of step S3. The pre-exponential factor of the reverse reaction is then determined to be 4.6×10^{14} mol/(s m³ washcoat) in order to satisfy the chemical equilibrium constant of step S3 at 400 K; i.e. $K_3(400\text{ K}) = k_{3,f}(400\text{ K})/k_{3,r}(400\text{ K})$. Together with the thermodynamically consistent activation energies, a ΔG balance of the above equation should be satisfied at any temperature. A similar ΔG analysis can be applied to Eq. (5). We used kinetic parameters from the study of Olsson et al. [5] for reaction steps S7, S8, S14, S15 and S16. Since both ΔG and ΔH balances were considered in the original paper, the ΔG calculation of Eq. (5) is not repeated here. Finally, the requirements of reversibility and mass action kinetics are not satisfied for other dependent reaction steps in our kinetic scheme so the ΔG analysis is not generally applicable.

2.4. Rate expressions and kinetic parameters

In this study, each reaction rate is formulated in the simplest form of the product of a rate constant and species concentrations

Table 3
Kinetic parameters used in simulations.

Step no.	A_f (mol m ⁻³ s ⁻¹)/ S_0	E_f (kJ/mol)	A_v (mol m ⁻³ s ⁻¹)	E_v (kJ/mol)
S1	7.5E9 [5] ^b	0.0 [5]	5.7E17 [5] ^b	114.5 [5]
S2	$S_0 = 0.046$ [42]	/	4.02E14 ^b	73
S3	4.02E12 ^b	60.0	4.6E14	143.7 ^a
S4	2.0E8 ^b	24.0 ^a	4.02E15 ^b	85.7 [17]
S5	4.02E14 [41]	11.5 [39]	6.28E15 [41]	74.9 [41]
S6	4.02E14 [41]	17.4 [39]	–	–
S7	–	–	4.0E16 ^b	130
S8	5.44E13 [5] ^b	107.8 [5]	4.0E14 [5] ^b	128.1 [5]
S10	8.0E14 ^b	117.0 ³³	2.0E17 ^b	146.5
S13	$S_0 = 1.0$ [37]	/	8.5E15 ^b	48.4 [37]
S14	4.7E8 [5] ^b	30.4 [5]	5.8E16 [5] ^b	209.4 [5]
S15	4.5E14 [5] ^b	101.3 [5]	2.5E14 [5] ^b	52.5 [5]
S16	8.0E9 [5] ^b	0.0 [5]	5.7E17 [5] ^b	97.9 [5]
S17	4.0E14	40.0	–	–
S18	4.0E14	30.0	–	–
S19	4.0E14	80.0	–	–
S20	8.0E14 ^b	60.0	4.0E15	109.8 ^a

Underlined parameters were adjusted to capture experimental trends.

^a Calculated from thermodynamic constraints.

^b Sensitive pre-exponential parameters.

with properly assigned orders. Table 2 compiles the rate expressions while Table 3 provides the values of the kinetic parameters. Most reactions in the model involve one or two reactants, which are surface and/or gaseous species. We assume mass action kinetics, unless otherwise specified. Exceptions are reactions that lump two or more elementary steps as discussed below. The model contains the following reaction types.

- Adsorption. The adsorption of H₂, O₂ and N₂O (forward reactions of S2, S4, S14) require two vacant Pt sites. According to the literature, H₂ adsorption is first order with respect to the concentration of vacant Pt sites [38,40]. This indicates that the molecular adsorption of H₂ is rate limiting and the decomposition to H–Pt is fast. We assume that O₂ adsorption is second order with respect to Pt vacant sites [38,40]. Similarly, we assume a second order dependence for N₂O adsorption. Compared with H₂, the non-zero adsorption activation energies of O₂ and N₂O listed in Table 3 indicate energy barriers during the adsorptive decomposition.
- Desorption. The desorption rates of O₂ and N₂ are assumed dissociative and the rates are second-order with respect to O and N coverage, respectively.
- Lumped reaction steps. The reaction steps S10, S17, S18 and forward S20 involve two surface species, whereas three surface sites of the same species are required (for example, 3 O–Pt in S17 and 3 OH–Pt in S18). We assume for these lumped steps that the rates are first order with respect to these species. Although this simplification is not supported by experimental data, it reduces the number of model unknowns and kinetic parameters, and is reasonable for the purpose this study. Finally, the forward reaction of step S19 and the reverse reaction of step S20 involve three surface species (including vacant sites). While each of these steps can be written as the stoichiometric combination of S3, S8 and S10 (S19 = S10 + 3S3; –S20 = S10 + S8), we consider them to be kinetically independent paths. While the true mechanisms are undoubtedly much more complex, we assume first order rate dependence on NH₃, NO and O adatom coverages and a zero order dependence on the vacant site coverage.

The rate expressions reported in Table 2 are defined using mole fractions for the gas species and coverages for the surface species. The total concentration and catalyst loading, as well as temperature dependence of reaction rates, are lumped into the rate constants. As such, all rate constants have the same units of mol/(s m³ washcoat).

The adsorption rate constants for H₂ and NH₃ are given by the product of the collision flux and a sticking coefficient:

$$k_i = S_{0,i} \times F_i \times \alpha_v = S_{0,i} \times \left[C_T (2\pi M_i / T / R)^{-0.5} \right] \times \alpha_v \quad (12)$$

where $S_{0,i}$ is the sticking coefficient of component i at zero coverage; F_i is the surface collision flux of pure i at gas phase concentration of C_T , M_i is molecular weight of component i , R is gas constant and α_v is active platinum surface area per unit volume of washcoat.

The Arrhenius expression is used for all other rate constants:

$$k_i = A_i \exp\left(\frac{-E_i}{RT}\right) \quad (13)$$

where A_i and E_i are the corresponding pre-exponential factor and activation energy, which are assumed independent of temperature and fractional surface coverage, respectively.

Kinetic parameters used in the simulations are summarized in Table 3. Where possible, literature values were used. In the case that literature data are conflicting, we chose studies more relative

to our study in terms of the reaction systems and operating conditions. Remaining parameters were estimated or adjusted to capture main experimental trends and to satisfy thermodynamic constraints. Activation energies of some steps were constrained by the enthalpic constraints as discussed in the previous section. For the first estimation, the pre-exponential factors not available in the literature were assigned a value of $4.0 \times 10^{14} \text{ mol}/(\text{s m}^3 \text{ washcoat})$; i.e., product of the active site concentration, 40 mol Pt/ m^3 washcoat, and the conventional 10^{13} s^{-1} for surface rate processes. Some parameters were adjusted during the simulations; these are noted in Table 3. It should be reiterated that no rigorous optimization work was carried out to fit experimental data in the parameter estimation of this study.

3. Simulation results and discussion

Model predictions and the comparison with experimental data from Clayton et al. [25] are presented and discussed in the following sections. Simulations were carried out using the isothermal short monolith model consolidated with the 17-step microkinetic model. The final reactor model comprised 14 state variables and algebraic equations (balance equations for N_2 and H_2O were eliminated because they were assumed inert in this study). The set of equations were solved using a pseudo-arc-length continuation method in order to get the full conversion and selectivity profiles including multiple solutions, which cannot be obtained by integrating the transient equations. All calculations were conducted on a personal computer equipped with an AMD 1.6 GHz CPU and a single curve could be obtained in just few seconds. This efficiency made the SMR model practically valuable.

3.1. NH_3/O_2 system

Conversion and selectivities are defined as

$$\text{NH}_3 \text{ conversion} = \left(1 - \frac{C_{\text{NH}_3,m}}{C_{\text{NH}_3,f}}\right) \times 100\% \quad (14)$$

The N-containing products are N_2O , NO and NO_2 , and N_2 , whose selectivities are defined by the following:

$$\text{N}_2\text{O selectivity} = \frac{2C_{\text{N}_2\text{O},m}}{C_{\text{NH}_3,f} - C_{\text{NH}_3,m}} \times 100\% \quad (15a)$$

$$\text{NO selectivity} = \frac{C_{\text{NO},m}}{C_{\text{NH}_3,f} - C_{\text{NH}_3,m}} \times 100\% \quad (15b)$$

$$\text{NO}_2 \text{ selectivity} = \frac{C_{\text{NO}_2,m}}{C_{\text{NH}_3,f} - C_{\text{NH}_3,m}} \times 100\% \quad (15c)$$

with the N_2 selectivity determined by an overall N balance. The stoichiometric number of the feed is defined as the weighted ratio of oxidant to reductant based on the overall reactions to favorable products (N_2 and H_2O here):

$$S_N = \frac{\text{NO} + 2\text{O}_2}{\text{H}_2 + 1.5\text{NH}_3} \quad (16)$$

Figs. 1 and 4 show the comparison of experimental data and predicted NH_3 conversion and selectivities to different N-containing species as a function of feed temperature for several feed compositions. The model captures the main experimental trends. The NH_3 oxidation system with excess O_2 ignites about 150°C , forming a complex mixture of N_2O , N_2 , NO, and NO_2 . S_N for all experiments is greater than 1 and O_2 is in excess. Under these conditions, the ignition curves for different O_2 concentration overlap each other. The solid curve in Fig. 1 was calculated for 0.2% O_2 feed. [Remark: the predicted NH_3 conversion is limited to 93.8%

due to the short monolith model assumption of complete back mixing.] The experimental conversion data in Fig. 1 suggest a very slight negative-order dependence on oxygen concentration. However, the model-predicted conversion was essentially independent of the oxygen concentration since the surface is primarily covered with N adatoms in this temperature range (Fig. 5).

The NO selectivity increases monotonically with temperature from about 250°C . Both N_2O and NO_2 selectivities exhibit maximum values, located at about around 250 and 400°C , respectively. The NO selectivity increases sharply with increased O_2 concentration and is then maintained at a constant level for O_2/NH_3 ratio greater than 2, whereas the N_2O and NO_2 selectivities increase more gradually with increased O_2 concentration. Notably, the model predicts a maximum NO selectivity for 500 ppm O_2 feed at 410°C , while experimental results showed a monotonic increase. Also, N_2O selectivity was experimentally observed over a wider temperature range than the model predictions. In spite of these quantitative deviations, the model predictions capture most of the experimental trends. The matching could be improved by rigorous optimization work, which is not the purpose of the current study.

Surface species coverages for 0.5% O_2 feed are shown in Fig. 5. At low temperature, the Pt surface is mostly covered by N adatoms with the balance being vacant Pt sites. The vacant sites enable the dissociative adsorption of O_2 , supplying O adatoms for the oxidative dehydrogenation of NH_3 to commence (step S17). At about 150°C , the oxygen coverage begins to increase sharply with temperature, igniting the system. At this temperature, surface NO is formed via reverse reaction of S8 ($\text{N} - \text{Pt} + \text{O} - \text{Pt}$), its coverage increasing to the level of 10^{-3} with increased temperature. Adsorbed NO is the key adsorbed species for N_2O and NO_2 formation, and therefore plays a very important role in the product distribution. According to the microkinetic model, surface NO is involved in seven reaction steps; S1, S3, S4, S8, S15, S19 and S20. The simulations show that, under these operating conditions, S1 (NO adsorption/desorption), S4 (N_2O adsorptive decomposition/formation), S8 (NO decomposition/formation) and S15 (NO_2 formation/decomposition) are faster than the remaining three, and the source term in the material balance of NO–Pt simplifies to:

$$R_{1,N} + R_{4,N} - R_{8,N} - R_{15,N} = 0 \quad (17)$$

where $R_{i,N}$ is the net rate of step i . The calculated net rates of the above four steps are plotted in Fig. 6 as a function of temperature for the 0.5% O_2 feed. It is seen that, after light-off at 150°C , the net formation rate of NO–Pt ($-R_{8,N}$) continues to increase. In the 150 – 250°C temperature range, NO formation is mainly balanced by its conversion to N_2O ($-R_{4,N}$), resulting in increasing N_2O selectivity. At about 250°C , NO desorption commences. The net rate of NO desorption ($-R_{1,N}$) increases with temperature and becomes the most important NO–Pt consumption term in Eq. (11). At the point, the N_2O formation rate and corresponding selectivity drop off. At a temperature of about 300°C , the formation of NO_2 ($R_{15,N}$) commences. The formation rate first increases and then decreases with temperature, a typical behavior controlled by the coupling of kinetic and thermodynamic effects. The formation of NO_2 is relatively slow compared to that of NO desorption (by about one order magnitude) and does not affect the overall rising trend of NO selectivity.

Fig. 7 compares the model predictions with experimental data in terms of N_2 , NO and NO_2 selectivities as a function of feed oxygen concentration at a fixed temperature (390°C). The calculated fractional coverages of several surface species are shown in Fig. 8. At very low oxygen concentration, the Pt surface is more than 99% vacant for oxygen and ammonia adsorption. NH_3 is partially oxidized to N_2 and H_2O , with the conversion determined

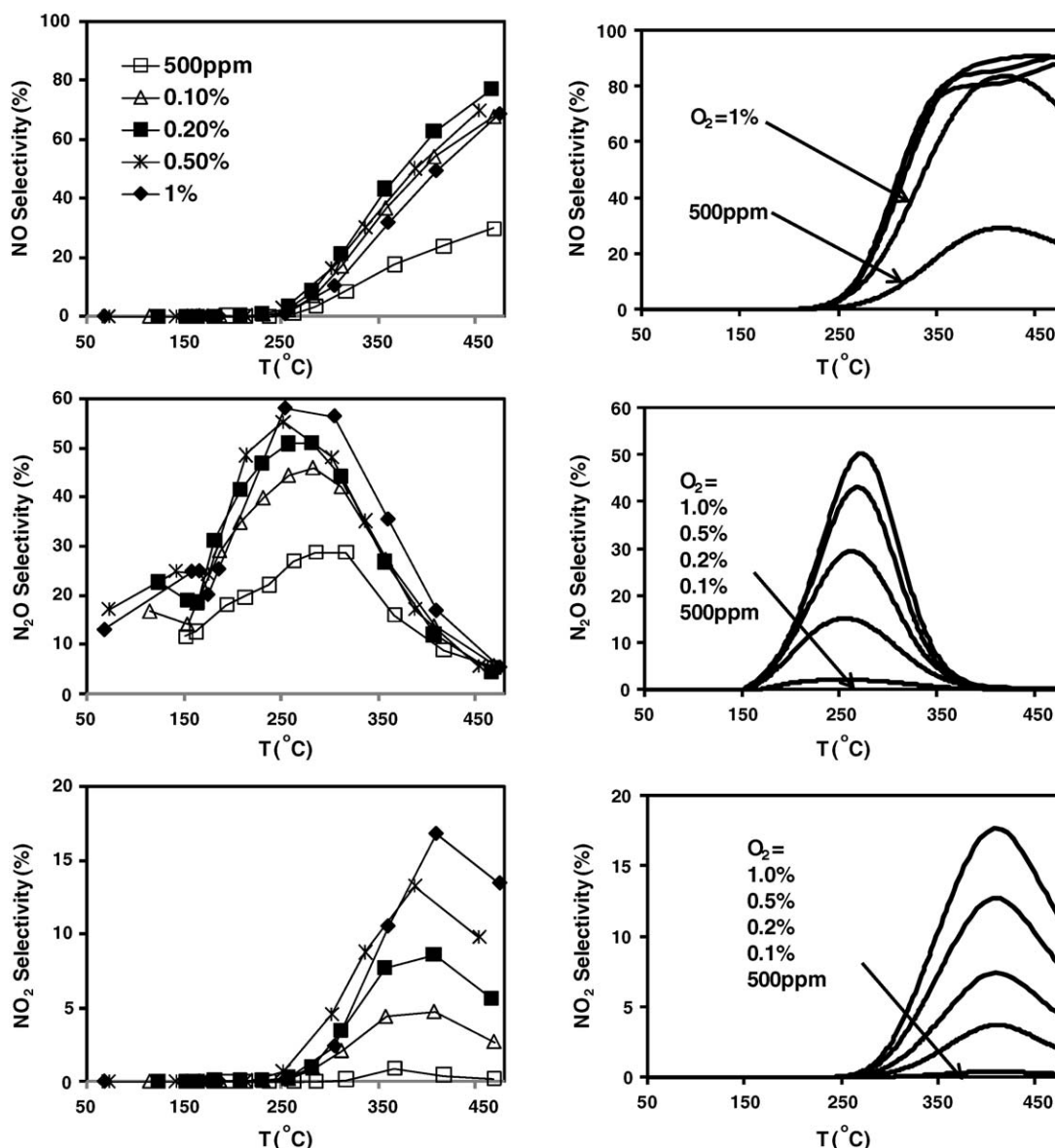
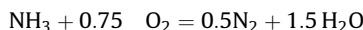


Fig. 4. Product selectivities of NH_3 oxidation as a function of feed temperature. NH_3 concentration is fixed at 500 ppm and O_2 concentration varies from 500 ppm to 1%. Experimental data are shown on the left side. Model predictions are shown on the right side.

by the oxygen supply according to the stoichiometric relationship of the overall reaction:



The coverage of N adatoms increases, whereas NH_3 -Pt decreases, with increased feed O_2 concentration. A transition occurs at S_N equal to 1, the stoichiometric O_2/NH_3 ratio of the above overall reaction. At the transition point, oxygen begins to occupy the Pt surface and becomes the dominant species, resulting in NO and NO_2 formation and a decrease in N-Pt coverage. Consequently, right after this point, N_2 (NO) selectivity decreases (increases) sharply with small increases in the O_2 concentration. The NO selectivity achieves a maximum value and then decreases gradually, which can be explained by the so called “oxygen poisoning” of platinum surface. The coverages of N-Pt and NO-Pt are of the same magnitude (10^{-2}) with the balance of the surface occupied by O-Pt. The further increase in O-Pt coverage leaves fewer Pt sites occupied by N adatoms, which are needed for NO formation. This results in a decrease in the NO-Pt coverage and NO selectivity. On the other

hand, while NO_2 -Pt coverage displays a maximum similar to that of NO-Pt, NO_2 selectivity monotonously increases with O_2 concentration. In order to explain this behavior, we consider the following additional effects: (1) NO_2 -Pt coverage is several magnitude order lower than the balance of O-Pt and is not directly affected by oxygen poisoning; (2) the decrease in NO-Pt coverage is a negative effect for NO_2 formation; (3) the decrease in platinum vacant sites (magnitude order of 10^{-2}) prevents NO_2 -Pt from being decomposed and shifts NO_2 adsorption equilibrium towards desorption, hence, being a positive effect. Both simulation and experimental results indicate that the factors favorable to overall NO_2 production dominate under the operating conditions. N_2O selectivity, the balance of the other three products, is maintained as a low level of around 10%. It is not shown in the figure.

3.2. NH_3/NO System

NO reduction by NH_3 , as mentioned earlier, may be important during the reduction/regeneration phase of the NO_x trap with H_2 as the reductant. The proposed microkinetic model accounts for

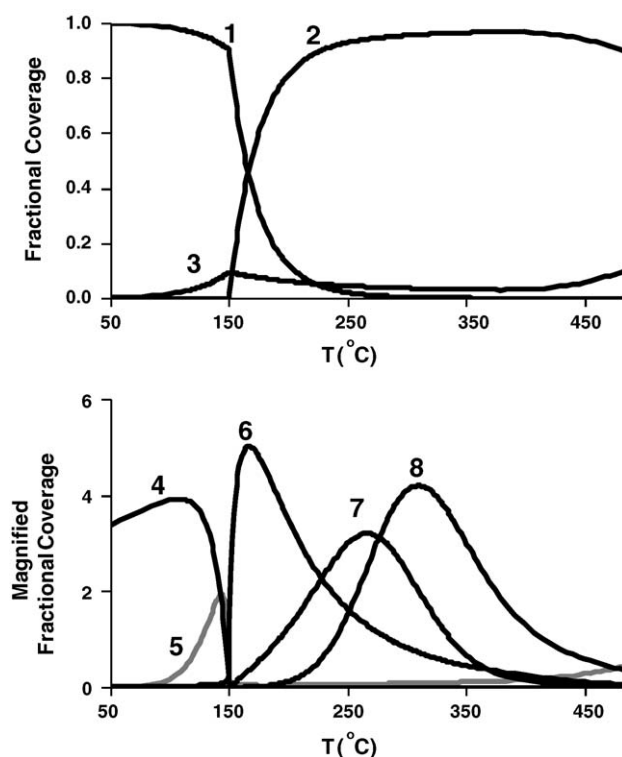


Fig. 5. Calculated fractional coverages of surface species during steady-state NH₃ oxidation as a function of temperatures (500 ppm NH₃ and 0.5% O₂ in the feed). (1) N-Pt, (2) O-Pt, (3) vacancy, (4) NH₃-Pt/10⁻⁵, (5) H-Pt/10⁻⁸, (6) OH-Pt/10⁻³, (7) NO-Pt/10⁻³, (8) NO₂-Pt/10⁻⁶. Line 5 is made light grey to be easily distinguished from other lines.

this reaction by steps S18 and S19. We used the model to predict steady-state conversion and product distribution of an equimolar NH₃/NO feed (500 ppm each, $S_N = 0.67$; excess NH₃). The results are compared with experimental data from Clayton et al. [25] in Fig. 2. Since both feed components are N-containing species, the N₂O and N₂ productions are evaluated by their effluent concentrations to avoid ambiguous definition of selectivities. It is interesting to note that the model has multiple solutions in the 115–170 °C temperature range. This rate multiplicity, resulting from the coupling of non-linear chemistry, occurs in the regime in which rapid NO reduction occurs, and has been referred to as a “surface explosion” in the literature [43]. Within this temperature range, the catalyst surface can be either exclusively occupied by NO or free for other surface species (reductant and/or products of the reduction), corresponding to the quenched branch and the ignited branch, respectively. While multiplicity was not confirmed

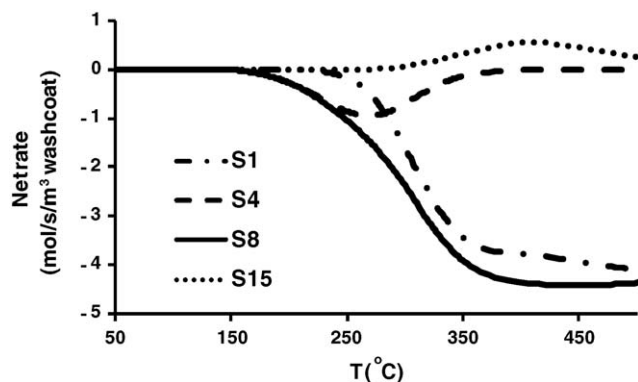


Fig. 6. Calculated net rates of steps S1, 4, 8 and 15 for NH₃ oxidation system with 0.5% O₂ feed.

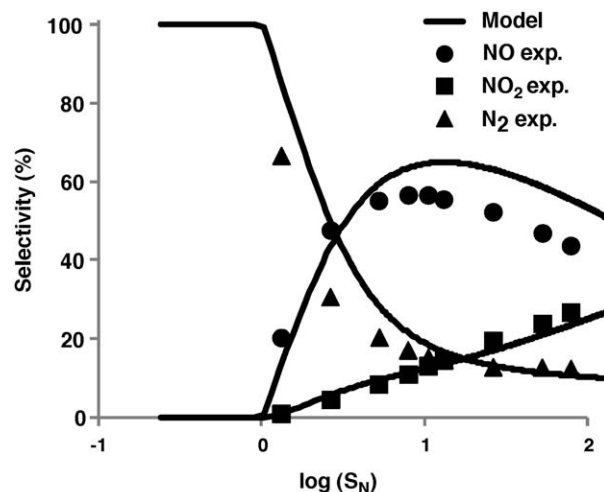
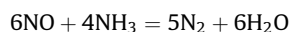


Fig. 7. Product selectivities of NH₃ oxidation as a function of the stoichiometric number at 390 °C. NH₃ concentration is fixed at 500 ppm. Solid lines are model predictions. Solid points are experimental data.

experimentally, the data do show extreme parametric sensitivity under the conditions for which the model predicts multiple rate states.

The calculated fractional coverages of the surface species plotted in Fig. 9(a) provide more detailed insight into the reaction pathways. At low temperature NO completely covers the surface and the conversion is negligible. A large increase in the conversion occurs abruptly at about 170 °C. The state of the catalyst goes from a NO-covered surface to one with a mixture of NO-Pt, N-Pt, and vacant sites. The vacant Pt sites enable the adsorption of NH₃, which reacts with NO, forming H₂O and N adatoms via reaction steps S18 and S19. Complete NO conversion is obtained with a very small temperature increase. NO and N coexist on the surface only in the temperature of range 110–200 °C, resulting in a relatively narrow window in which N₂O selectivity is non-zero, although the model predicts a higher N₂O peak than observed experimentally. The predicted peak is very steep, underscoring the non-linear kinetic behavior. From 200 to 400 °C, the reaction system is dominated by the following overall reaction:



While NO can be fully reduced to N₂, the NH₃ conversion is limited to 67%. NH₃ conversion and N₂ production increase at even higher temperature due to the emergence of NH₃ decomposition.

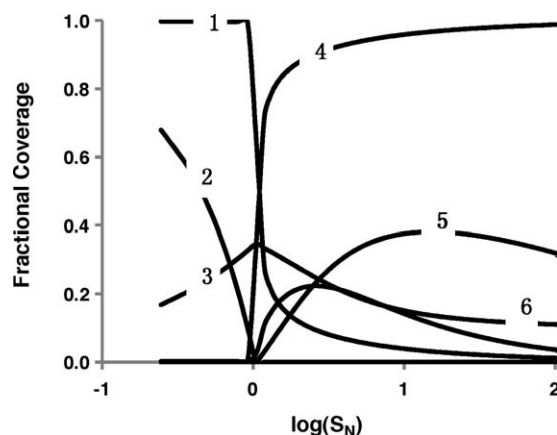


Fig. 8. Calculated fractional coverage of surface species during steady-state NH₃ oxidation as a function of O₂ concentration. (1) Vacancy, (2) NH₃-Pt/10⁻⁵, (3) N-Pt/10⁻², (4) O-Pt, (5) NO₂-Pt/10⁻⁵ and (6) NO-Pt/10⁻².

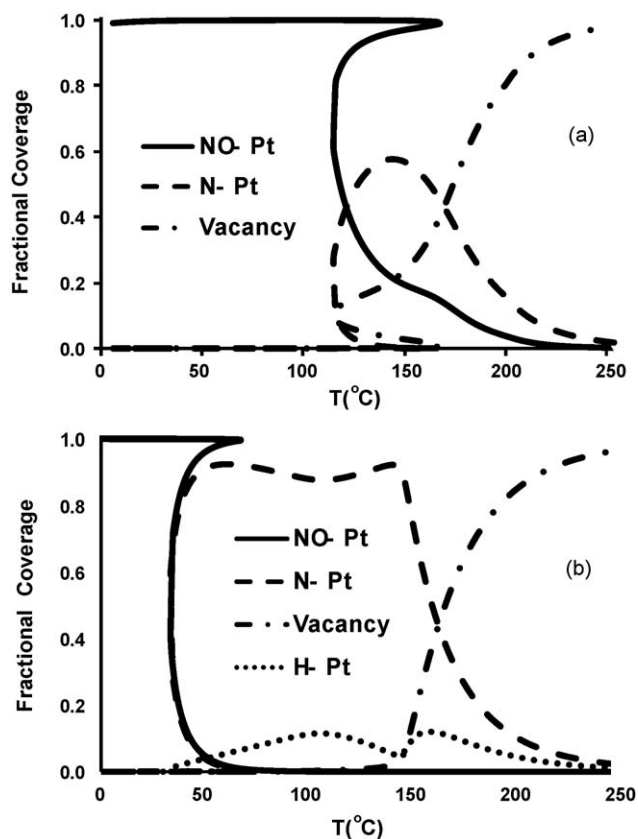
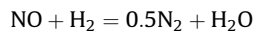


Fig. 9. Calculated fractional coverages of major surface species around ignition temperature of rapid NO reduction, showing surface explosion. (a) NH_3/NO , 500 ppm each; (b) $\text{NH}_3/\text{H}_2/\text{NO}$, 500 ppm each.

3.3. $\text{NH}_3/\text{H}_2/\text{NO}$ System

Finally, the model was used to study the steady-state behavior of an equimolar $\text{NH}_3/\text{H}_2/\text{NO}$ feed as a function of temperature. The predicted effluent concentrations of all gas species, except for O_2 and NO_2 , which are negligible under these rich conditions ($S_N = 0.4$), are directly compared with experimental measurements in Fig. 3. The agreement between model and experiment is generally good. Some of the same features such as rate multiplicity, NH_3 decomposition at high temperature, and mass transfer limitation on conversion (discussed below) hold true here as in the NH_3/NO system. Both experiments and simulations showed that H_2 is more effective than NH_3 as the NO reductant. The ignition temperature for NO reduction by H_2 is about 70°C , much lower than that by NH_3 (see Section 3.2). This is due to the lower activation energy of the forward reaction of S3 (60 kJ/mol) than that of S19 (80 kJ/mol). NO bond scission occurs through reaction with H adatoms at low temperature, forming N adatoms. This is the crucial step for the ignition of NO reduction by H_2 . The fractional coverages of major surface species are also shown in Fig. 9(b) for comparison with the ignition of NH_3/NO system. Of particular note is that H adatoms, unlike adsorbed NH_3 in the NH_3/NO system, occupy a significant fraction of the Pt sites over a wide temperature range. Ignition can also be affected by feed composition. A previous study showed that an increase in the feed H_2 concentration reduces the ignition temperature [17]. The same study showed that further increases in H_2 overcome NO in occupying the Pt sites even at low temperature, i.e. no surface explosion, and the rate multiplicity disappears. After ignition, in addition to N_2O , NH_3 is also formed and the production of both decline at around 180°C . This interesting phenomenon is successfully captured by reaction step

S20 with the same activation energy as S3. In the $180\text{--}400^\circ\text{C}$ temperature range, NH_3 practically acts as an inert component. NO is completely reduced by equimolar H_2 according to the following overall reaction:



At even higher temperature, NH_3 is decomposed to N_2 and H_2 .

3.4. Influence of external mass transfer

In the short monolith reactor model, gas concentrations in the bulk phase are distinguished from those in the washcoat and, therefore, radial (transverse) mass transfer effects are properly taken into account. In this section we assess the importance of external mass transfer by examining the concentration ratio for component i :

$$\text{CR}_i = \frac{C_{i,s}}{C_{i,m}} \quad (18)$$

An example calculation of CR_i is shown in Fig. 10 for the ternary component $\text{NH}_3/\text{H}_2/\text{NO}$ system as a function of temperature. It is seen that at temperatures less than the ignition temperature, CR_i values are very close to unity, indicating negligible external mass transfer effects. As expected, the conversion is limited by kinetics in this regime. After ignition, the CR value for NO decreases sharply with increased temperature. At complete conversion, NO concentration in the washcoat is smaller than that in the bulk phase by several orders of magnitude, a clear indication of strong external mass transfer limitations. The CR value of H_2 , the other major

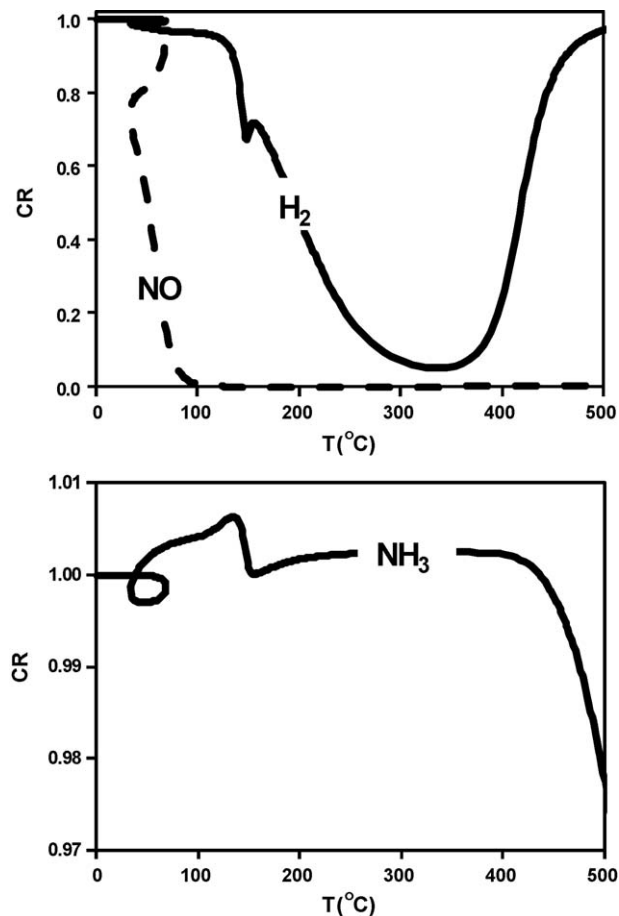


Fig. 10. Calculated CR values of NO, H_2 and NH_3 as a function of temperature, showing external mass transfer effects.

reactant, however, decreases more gradually with increased temperature, similar to the trend of its gradually increased conversion (Fig. 3). In the high conversion regime in which N_2 and H_2O are the major products, the CR of H_2 does not approach zero as in the case of NO, because H_2 has a higher mass transfer coefficient (Table 1). While the feed contains equimolar H_2 and NO, the higher mass transfer coefficient of H_2 creates a local rich condition in the washcoat, resulting in some NH_3 formation under these conditions. In the previous NO/ H_2 study, we examined the effects of feed composition on the product distribution. The calculated transition point from N_2 to NH_3 occurs at an S_N slightly less than 1, which is also due to this local enrichment of H_2 in the washcoat [17]. At even high temperatures, H_2 becomes a product of NH_3 decomposition, and the CR value increases together with a decreased conversion. The NH_3 CR exhibits values greater than as well as less than unity under different temperatures, corresponding to the two overall roles of NH_3 in this system, product and reactant, respectively.

In general, in the ignited and near complete conversion regime, the supply of at least one of the reactants is limited by external mass transfer. The concentration of this reactant in the washcoat is essentially 0 and Eq. (1) for this component reduces to

$$\frac{X_{i,m} - X_{i,f}}{\tau_c} + \frac{k_{c,i}}{R_\Omega} X_{i,m} = 0 \quad (1a)$$

which is decoupled from the reaction network and can be independently solved without any kinetic information. Even for the reactants and products not limited by mass transfer, the concentrations in the washcoat can still deviate considerably from those in the bulk. Since only the concentrations in the washcoat are pertinent to the catalysts, neglecting mass transfer effects will result in significant errors in the estimation of kinetic parameters. Recent work in our group using low-dimensional modeling shows that the diffusion within the washcoat can have even more significant effects than external mass transfer in catalytic monoliths [44]. This will be reported in a future publication as it relates to NOx storage and reduction.

The above discussion also points to the importance of care in choosing experimental data for kinetic parameter estimation of catalytic reaction systems. Low conversion data are more kinetically relevant, but are typically difficult to measure. On the other hand, high conversion data are more reliable but may contain no kinetic information. Among the bunch of experimental data, only a small section are relevant and valuable for kinetic parameter estimation. These points could be where the system is ignited, where the system is quenched, where the formation of a particular product commences, hits the maximum and fades away. For this reason, we did not carry out any optimization work in this study. The fact that our simple model captures all major experimental trends also illustrates that no additional kinetic information can be safely obtained from similar experimental data, however many points.

3.5. Sensitivity of kinetic parameters

A systematic sensitivity study of pre-exponential factors was carried out to identify the critical kinetic steps for a range of different conditions. While it is impractical to present the detailed results here, the main conclusions are summarized as below. A more detailed presentation of the sensitivity study will be reported elsewhere [45].

- Effluent compositions are sensitive to rates of only a subset of the reaction steps. These are noted in Table 3. The remaining reaction steps are either too fast to be rate limiting or too slow to be significant.

- Rich conditions ($\text{NH}_3/\text{H}_2/\text{NO}$ system). Ignition is controlled by the desorption of NO which provides vacant Pt sites for H_2 adsorption. The main source of N adatoms, which are crucial for both N_2O and N_2 formation, is NO bond scission through reaction with H adatoms (S3) at low temperature, while direct NO decomposition dominates at higher temperature. The selectivity of N_2O and N_2 in the temperature range of 70–200 °C is mainly controlled by N_2 desorption (reverse of S7); NH_3 formation in the intermediate temperature range is controlled by reaction S20 ($\text{NO} - \text{Pt} + 3\text{H} - \text{Pt} \leftrightarrow \text{NH}_3 - \text{Pt} + \text{O} - \text{Pt} + 2\text{Pt}$), a reaction route parallel and competitive with S3. The decomposition of adsorbed NH_3 to N and H adatoms (reverse S10 reaction) and H_2 desorption have significant effects on the overall ammonia decomposition reaction ($\text{NH}_3 = 0.5\text{N}_2 + 1.5\text{H}_2$) at temperatures exceeding 350 °C.
- Lean conditions (NH_3/O_2). The oxidation of NH_3 via reaction steps S17 and S18 is preferred over the route by ammonia decomposition (S10 reverse reaction) and hydrogen oxidation (S2, S14, S5 and S6). The ignition is controlled by the desorption of N adatoms, the primary surface species before ignition (Fig. 5), to N_2 , the major product at low temperature; The N_2 desorption rate (S7 reverse reaction) has a significant effect on the product distribution since N adatoms are needed for NO, N_2O and NO_2 formation. NO formation (S8 reverse reaction) is a critical step for N_2O and NO_2 production while NO decomposition (S8) while important is not in equilibrium with its reverse reaction in the temperature range of this study. On the other hand, NO adsorption/desorption (S1), N_2O adsorptive decomposition/formation (S4), NO_2 formation/decomposition (S15) and adsorption/desorption (S16) are fast steps and approach thermodynamic equilibrium. At intermediate temperatures (200 °C < T < 400 °C) the Pt surface is covered with oxygen adatoms (Fig. 5) which inhibit the formation of NO and NO_2 . At temperature exceeding 350 °C, oxygen desorption commences, freeing up Pt sites which increases NO_2 formation rate. Once ignited, the NH_3 oxidation is limited by external mass transfer of NH_3 to the surface.

4. Conclusions

In this study we have developed a microkinetic model describing the steady-state reactions between NO, H_2 , O_2 , and NH_3 on Pt. The microkinetic model consisting of both elementary and lumped steps is based on previously published experimental findings and thermodynamic analyses. The model consolidated into a “short monolith reactor” formulation predict all major experimental trends of NH_3/O_2 , NH_3/NO and $\text{NH}_3/\text{H}_2/\text{NO}$ systems without involving rigorous optimizations. Calculated coverages of surface species and reaction rates of competitive pathways provide insightful interpretations of conversions and product distribution under different conditions. Rate multiplicity is predicted for NO reduction by H_2 and NH_3 , as a result of the strong coupling of non-linear kinetics. It was found that external mass transfer has significant effects on the concentrations in the washcoat of a catalytic monolith reactor and has to be considered during the estimation of kinetic parameters and interpretation of the results.

Ongoing work in our group involves the development of a full transient model for the lean NOx trap. Understanding the steady-state catalytic kinetics is essential for interpreting the data for the more complex NOx storage and reduction. While storage and interfacial chemistry are unique features during NSR, undoubtedly much of the catalysis that occurs follows from that observed during steady-state operation. In future work, we will apply the results of this work in the modeling of the lean NOx trap reactor.

Acknowledgements

The work reported was supported by the U.S. DOE National Energy Technology Laboratory (DE-FC26-05NT42630).

References

- [1] N. Ladommatos, S. Abdelhalim, H. Zhao, *Appl. Therm. Eng.* 18 (11) (1998) 963–980.
- [2] M. Koebel, M. Elsener, M. Kleemann, *Catal. Today* 59 (3–4) (2000) 335–345.
- [3] V.G. Komvokis, E.F. Ilopoulou, I.A. Vasalos, K.S. Triantafyllidis, C.L. Marshall, *Appl. Catal. A: Gen.* 325 (2) (2007) 345–352.
- [4] N. Takahashi, H. Shinjoh, T. Iijima, T. Suzuki, K. Yamazaki, K. Yokota, H. Suzuki, N. Miyoshi, S. Matsumoto, T. Tanizawa, T. Tanaka, S. Tateishi, K.N. Kasahara, *Catal. Today* 27 (1996) 63–69.
- [5] L. Olsson, B. Westerberg, H. Persson, E. Fridell, M. Skoglundh, B. Andersson, *J. Phys. Chem. B* 103 (1999) 10433–10439.
- [6] K.S. Kabin, P. Khanna, R.L. Muncrief, V. Medhekar, M.P. Harold, *Catal. Today* 114 (1) (2006) 72–85.
- [7] K.S. Kabin, R.L. Muncrief, V. Medhekar, M.P. Harold, *Catal. Today* 96 (1–2) (2004) 79–89.
- [8] Edmondson, Gail, Diesel Gets Cleaner and Greener, *Business Week*, 9 February 2006, http://www.businessweek.com/autos/content/feb2006/bw20060208_539996.htm.
- [9] M. Hemingway, in: *Proceedings of the DEER Conference*, Detroit, USA, 2006.
- [10] H. Hu, in: *Proceedings of the DEER Conference*, Detroit, USA, 2006.
- [11] T. Morita, N. Suzuki, N. Satoh, K. Wada, H. Ohno, Study on Low NO_x Emission Control Using Newly Developed Lean NO_x Catalyst for Diesel Emissions, SAE, 2007, pp. 1–7.
- [12] H.G. Stenger Jr., J.S. Hepburn, *Energy Fuels* 1 (5) (1987) 412–416.
- [13] H. Hirano, T. Yamada, K.I. Tanaka, J. Siera, P. Cobden, B.E. Nieuwenhuys, *Surf. Sci.* 262 (1–2) (1992) 97–112.
- [14] H. Hirano, T. Yamada, K.I. Tanaka, J. Siera, B.E. Nieuwenhuys, *Stud. Surf. Sci. Catal. (New Front. Catal. A)* 75 (1993) 345–357.
- [15] T.P. Kobylinski, B.W. Taylor, *J. Catal.* 33 (3) (1974) 376–384.
- [16] M. Shelef, H.S. Gandhi, *Ind. Eng. Chem. Product Res. Dev.* 11 (1) (1972) 2–11.
- [17] J. Xu, R. Clayton, V. Balakotaiah, M.P. Harold, *Appl. Catal. B: Environ.* 77 (2008) 395–408.
- [18] L. Cumaratanunge, S.S. Mulla, A. Yezerets, N.W. Currier, W.N. Delgass, F.H. Ribeiro, *J. Catal.* 246 (1) (2007) 29–34.
- [19] K. Otto, M. Shelef, J.T. Kummer, *J. Phys. Chem.* 74 (13) (1970) p2690.
- [20] K. Otto, M. Shelef, *Prep. Am. Chem. Soc., Div. Petrol. Chem.* 18 (3) (1973) 443–451.
- [21] J.E. DeLaney, W.H. Manogue, in: *Proceedings of the 5th International Congress on Catalysis*, 1973, pp. 267–278.
- [22] G.L. Bauerle, S.C. Wu, K. Nobe, *Ind. Eng. Chem. Prod. Res. Dev.* 14 (2) (1975) 123–130.
- [23] K. Otto, M. Shelef, J.T. Kummer, *J. Phys. Chem.* 75 (7) (1971) 875–879.
- [24] J.L. Gland, V.N. Korchak, *J. Catal.* 55 (3) (1978) 324–336.
- [25] R. Clayton, M.P. Harold, V. Balakotaiah, *Appl. Catal. B: Environ.* 81 (3–4) (2008) 161–181.
- [26] J.P. Breen, R. Burch, C. Fontaine-Gautrelet, C. Hardacre, C. Rioche, *Appl. Catal. B: Environ.* 81 (1–2) (2008) 150–159.
- [27] R. Clayton, M.P. Harold, V. Balakotaiah, *Appl. Catal. B: Environ.* 84 (2008) 616–630.
- [28] V.A. Sadykov, L.A. Isupova, I.A. Zolotarevskii, L.N. Bobrova, A.S. Noskov, V.N. Parmon, E.A. Brushtein, T.V. Telyatnikova, V.I. Chernyshev, V.V. Lunin, *Appl. Catal. A: Gen.* 201 (1) (2000) 59–87.
- [29] L. Olsson, H. Persson, E. Fridell, M. Skoglundh, B. Andersson, *J. Phys. Chem. B* 105 (2001) 6895–6896.
- [30] M. Sharma, M.P. Harold, V. Balakotaiah, Analysis of Storage and Reduction of LNT for Diesel Engine Exhaust Treatment, SAE International, 05FFL-218, 2005.
- [31] R.S. Larson, J.A. Pihl, V.K. Chakravarthy, T.J. Toops, C.S. Daw, *Catal. Today* 136 (2008) 104–120.
- [32] P. Koci, F. Plat, J. Stepanek, M. Kubicek, M. Marek, *Catal. Today* 137 (2008) 253–260.
- [33] A. Lindholm, N.W. Currier, J. Li, A. Yezerets, L. Olsson, *J. Catal.* 258 (2008) 273–288.
- [34] V. Balakotaiah, N. Gupta, D.H. West, *Chem. Eng. Sci.* 55 (22) (2000) 5367–5383.
- [35] D.C. Ford, Y. Xu, M. Mavrikakis, *Surf. Sci.* 587 (2005) 159–174.
- [36] D.G. Loffler, L.D. Schmidt, *J. Catal.* 41 (3) (1976) 440–454.
- [37] J.J. Vajo, W. Tsai, W.H. Weinberg, *J. Phys. Chem.* 89 (15) (1985) 3243–3251.
- [38] M.Y. Smimov, V.V. Gorodetskii, J.H. Block, *J. Mol. Catal. A: Chem.* 107 (1996) 359–366.
- [39] E. Shustorovich, A.T. Bell, *Surf. Sci.* 289 (1) (1993) 127–138.
- [40] J. Warnatz, M.D. Allendorf, R.J. Kee, *Combust. Flame* 96 (1994) 393–406.
- [41] O. Deutschmann, R. Schmidt, F. Behrendt, J. Warnatz, *Symp. (Int.) Combust./Combust. Inst.* 26 (1996) 1747–1754.
- [42] M. Rinnemo, O. Deutschmann, F. Behrendt, B. Kasemo, *Combust. Flame* 111 (4) (1997) 312–326.
- [43] M.W. Lesley, L.D. Schmidt, *Surf. Sci.* 155 (1) (1985) 215–240.
- [44] S. Joshi, V. Balakotaiah, M.P. Harold, *AIChE J.* (2009), in press.
- [45] J. Xu, PhD Dissertation, University of Houston, in progress (2009).